ACS Catalysis

ACS EDITORS' CHOICE

pubs.acs.org/acscatalysis

Research Article

$CuFeO_2$–Water Interface under Illumination: Structural, Electronic, and Catalytic Implications for the Hydrogen Evolution Reaction

Matteo Ferri,[§] Joshua David Elliott,[§] Matteo Farnesi Camellone, Stefano Fabris, and Simone Piccinin*

Cite This: *ACS Catal.* 2021, 11, 1897–1910

Read Online

ACCESS | Metrics & More | Article Recommendations | Supporting Information

ABSTRACT: $CuFeO_2$ is a *p*-type semiconductor that has been recently identified as a promising photocathode material for photoelectrochemical water splitting. $CuFeO_2$ can absorb solar light and promote the hydrogen evolution reaction (HER), even though the photocurrents achieved so far are still well below the theoretical upper limit. While several experimental and theoretical works have provided a detailed characterization of the bulk properties of this material, surfaces have been largely unexplored. In this work, we perform first-principles simulations based on DFT to investigate the structure, electronic properties, and thermodynamic stability of $CuFeO_2$ surfaces both in vacuum and in an electrochemical environment. To estimate the alignment of the band edges on the electrochemical scale, we perform ab initio molecular dynamics in explicit water, unraveling the structure of the solid/liquid interface for various surface terminations. We consider the system both in the dark and under illumination, showing that light absorption can induce partial reduction of the surface, giving rise to states in the gap that can pin the Fermi level, in agreement with recent measurements. Using the free energy of adsorption of atomic hydrogen as a descriptor of the catalytic activity for the HER, we show that hydride species formed at oxygen vacancies can be highly active and could therefore be an intermediate of reaction.

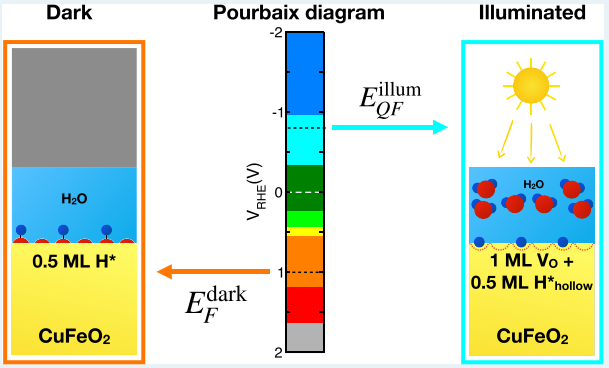

KEYWORDS: *photoelectrochemistry, density functional theory, hydrogen evolution reaction, Pourbaix diagram, level alignment, ab initio molecular dynamics, photocathode, aqueous interfaces*

INTRODUCTION

Splitting water molecules into molecular hydrogen and oxygen using photoelectrochemical (PEC) cells represents a promising route toward efficient conversion of solar radiation into chemical fuels.[1] Broadly speaking, water-splitting PEC cells are composed of two electrodes immersed in an aqueous electrolyte with one or both electrodes able to absorb solar radiation and generate charge carriers; photogenerated holes oxidize H_2O molecules at the anode producing O_2, releasing protons in solution, while electrons reduce protons to H_2 at the cathode. The so-called tandem cell setup where both electrodes can absorb light increases the flexibility in the design of PEC cells by incorporating photoactive n-type and p-type materials for the anode and cathode, respectively.

In the design of tandem PEC cells, transition metal oxides (TMOs) naturally emerge as leading candidates for both electrodes. Typically, TMOs are versatile and non-toxic and comprise earth abundant elements. Semiconducting TMOs offer a diverse range of electronic properties such that, at least in principle, each electrode can be tailored to the band gap and absolute energy level alignment appropriate for each electrochemical half-reaction.

Copper oxide (Cu_2O), a p-type semiconductor, has a band gap and first optical transition (1.77 and 2.17 eV, respectively[2]) well suited for visible light adsorption, and the position of the conduction band edge is ideally aligned for the electron transfer reactions associated with the formation of H_2. However, in spite of these promising properties, the redox potentials for the reduction and oxidation of Cu_2O lie within the band gap and consequently Cu_2O electrodes suffer from photodegradation in aqueous environments, ultimately making them unsuitable for PEC devices.[3−5]

Leveraging the benefits of Cu_2O, attention has turned to other copper-based TMOs for the photocathode and in particular, most recently, to the p-type copper-iron delafossite $CuFeO_2$ (CFO), which is stable under operation in aqueous electrolytes.[6−12] Like Cu_2O, CFO has a small band gap (1.5 eV) and energetic alignment of the conduction band edge

Received: November 19, 2020
Revised: January 5, 2021
Published: February 3, 2021

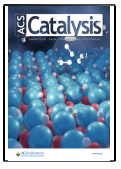

suitable for the HER[11] as well as a charge-transfer excitation between O 2p and Fe 3d states within the visible part of the electromagnetic spectrum.[13,14] CFO is composed of earth abundant elements, and different techniques for its growth and synthesis have been reported, including solid-state reactions,[15] electrodeposition,[6] pulsed laser deposition,[16] and sol−gel synthesis.[7] It should be noted that CFO thin films synthesized with a scalable, solution-based sol−gel method on top of a fluorine-doped tin oxide substrate showed good light absorption properties and favorable band-edge positions.[7,9]

Despite these favorable properties, CFO photocathodes exhibit maximum photocurrent densities of just 0.85 mA cm^{-2},[17−19] one order of magnitude under the theoretical limit.[19] Understanding and ameliorating this low photocurrent density has become the main focus of research into CFO photocathodes. The relatively poor performance of CFO photocathodes was understood to be linked to Fermi-level pinning at the solid−liquid interface.[11,20] The origin of these states, located at around 0.6 eV above the valence band, was first attributed to the presence of metal hydroxyl groups on the surface,[11] and later to the formation of bulk Fe^{3+}/Fe^{2+} polaronic levels.[20] However, a recent investigation of the CFO performance bottlenecks also highlighted short photogenerated electron diffusion lengths and polaron-mediated recombination as additional potential obstacles to be overcome.[19]

First-principles calculations can provide valuable insights into the operation of CFO photocathodes. Previously, simulations have been used to characterize the magnetic properties of CFO,[21,22] and more recently, these investigations have shifted, focusing instead on the electronic properties related to the CFO photocathodic performance.[14,19,23−25] Despite this interest, the nature of the electrode surface when exposed to an aqueous environment, which can be a large driving force in the overall photoelectrochemical properties, has yet to be reported either from theory or experimental work. This is surprising since, from a theoretical perspective, CFO surfaces have been the subject of investigation for CO_2 reduction.[26,27] Recent theoretical work has instead addressed the stability and propensity for defect formation in the bulk phase in dry and electrochemical conditions as well as the bulk electronic properties.[23,24] It was found that the liquid environment acts to stabilize the bulk CFO phase relative to other oxides in the region corresponding to experimental measurement, but the analysis does not account for different exposed surface stabilities, chemistry, or reconstructions.

We demonstrate in this work that the role of the interface between CFO surfaces and the electrolyte in the band-edge alignment cannot be overlooked. Here, we report the first ab initio molecular dynamics simulations of CFO surfaces in contact with water. Modeling explicitly the solid/liquid interface allows us to predict the position of the conduction band edge for various surface termination. By coupling this information with the Pourbaix diagram computed at the same level of theory, we introduce a novel approach to predict which surface structures are energetically favorable both in the dark and under illumination. This enables us to provide insights into the origin of Fermi level pinning and identify reaction intermediates of a light-driven HER.

COMPUTATIONAL METHODS

The density functional theory (DFT) calculations have been carried out using the PW.X code of the Quantum ESPRESSO suite[28,29] with optimized norm-conserving Vanderbilt pseudopotentials.[30,31] We used a plane-wave energy cutoff of 80 Ry (∼1088 eV). The Brillouin zones of (0001) and $(11\bar{2}0)$ surfaces were sampled with 4 × 2 × 1 and 3 × 1 × 1 grids of *k*-points, respectively.

For the treatment of electron exchange and correlation, we applied the Perdew−Burke−Ernzerhof (PBE) functional[32] with Hubbard *U* corrections,[33−35] and the value of $U_{eff} = U - J = 4.1$ eV for the Fe ions has been computed in our previous work[23] following the standard linear response[36] and self-consistency[37,38] protocol applied to the bulk system.

The surfaces were modeled using symmetric slabs with two identical terminations in order to avoid the formation of a net dipole moment within the unit cell. The slabs were periodically replicated with 12 Å of vacuum in the direction perpendicular to the surface to avoid spurious interactions between periodic replicas. For the (0001) surface, we found that a thickness of ∼15 Å, corresponding to three FeO_6 layers, yields surface energies converged to within 3 meV/$Å^2$, while for the $(11\bar{2}0)$ surface, a 6 Å thick slab composed of 5 layers is sufficient to converge the surface energy to within 1 meV/$Å^2$.

As shown in Figure S1, we have considered an antiferromagnetic arrangement of the Fe ions in the bulk crystal that we cut to construct the slabs. The bulk antiferromagnetic structure consists of layers of Fe atoms with a zero net magnetization in which each layer is formed by rows of atoms with opposite magnetization. In the resulting $(11\bar{2}0)$ slabs, each layer is uniformly magnetized but consecutive layers have opposite magnetization, while in the (0001) slabs, the overall magnetization is zero since each layer contains an equal number of oppositely spin-polarized Fe ions, resembling the bulk structure.

To compute the band alignment, we follow the three-step approach introduced by Guo et al.[39] First, we obtain the valence and conduction band edges of the bulk material aligned to the average electrostatic potential of the bulk unit cell, which is commonly set to zero in periodic boundary condition codes. We have recently determined that the hybrid PBE0 functional provides the best description of the electronic structure of bulk CFO, specifically, when an optimized fraction of exact exchange derived from the materials dielectric function is applied.[24] Here, these calculations have been replicated with the CP2K code[40] using a hexagonal 4 × 4 × 1 supercell, containing 192 atoms, sampling the Brillouin zone only at the Γ point.

Second, the standard hydrogen electrode (SHE) redox level must be aligned with the average electrostatic potential of bulk liquid water. A computational version of the SHE has been reported as the reduction potential of a hydronium ion into gaseous hydrogen,[41,42] while the alignment between SHE and the average electrostatic potential of bulk water has been computed by Ambrosio et al.,[43] who found the vacuum level to be 3.69 eV higher in energy than the average electrostatic potential of water and the SHE, 4.56 eV below the vacuum level.[43] We note that this value is in good agreement with the SHE value proposed by Trasatti, 4.44 eV.[44] Since we employed the same computational setup adopted in ref 43, we used the values computed therein to align the SHE and the vacuum level with the average electrostatic potential of bulk water.

Finally, to align the energy levels of bulk water and bulk oxide, we compute the profile of the electrostatic potential across the CFO/water interface, which depends on the specific surface termination considered. We do this by sampling the

https://dx.doi.org/10.1021/acscatal.0c05066
ACS Catal. 2021, 11, 1897−1910

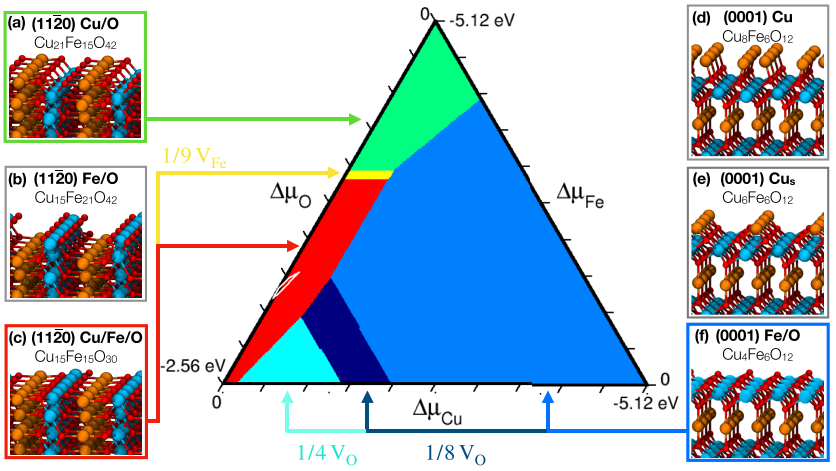

Figure 1. (a–f) Side views detailing the different termination stoichiometries and their optimized geometries, which are screened in our simulations. Orange, blue, and red spheres represent Cu, Fe, and O atoms, respectively. In the central portion, the ternary plot indicates the surface with the lowest surface energy for each triplet of chemical potentials. The figures of crystal structures have been generated with the VMD molecular graphics viewer.[55]

system using ab initio molecular dynamics (AIMD) simulations and time-averaging the electrostatic potential through the analysis of several snapshots of the AIMD.

To this end, we replicated the slabs in the *xy* plane to form 4 × 2 × 1 and 2 × 1 × 1 supercells for the (0001) and (11$\bar{2}$0) surfaces, respectively. These slabs were interfaced with 15 Å of explicit water, which corresponds to simulations cells containing 59 and 77 water molecules for the (0001) and (11$\bar{2}$0) the surface, respectively. In addition, a vacuum region of ∼10 Å divides the explicit water and the periodic replica of the bottom surface. We performed AIMD simulations with the Quickstep code[40] of the CP2K software package, which adopts a mixed Gaussian and plane-wave basis set. We employed the molecularly optimized (MOLOPT) DZVP-SR Gaussian basis set for the wavefunctions and a plane-wave cutoff of 500 Ry for the charge density, while the Goedecker–Teter–Hutter (GTH) pseudopotentials[45] were used to model the electron–ion interactions. We adopted the DFT+*U* scheme using the rVV10 functional, which provides a correct description of the structural properties of the explicit water without changing the electronic structure of CFO, and we set the value of the parameter *b* in the rVV10 functional to 9.3, as suggested in recent studies.[46−48] The Hubbard *U* correction on the *d* states of Fe was set equal to 3.3 eV, which provides a good description of the octahedral Fe^{3+} in Fe_2O_3.[49]

Although the band edges of bulk CFO were computed with the hybrid PBE0 functional, we performed the AIMD simulation with the PBE+*U* approach since it has been shown that the electrostatic alignment is weakly dependent on the employed functional with discrepancies of the order of 0.01 eV.[39] We run the AIMD simulations in the *NVT* ensemble for a total simulation time between 8 and 15 ps, setting the temperature to 360 K through a velocity rescaling (CSVR) thermostat.[50] The mass of the hydrogen atoms was set equal to the mass of deuterium, 2 amu, and we adopted a time step of 1 fs. The profile of the electrostatic potential across the CFO–water interface is determined by planar averages on planes parallel to the surface and by averaging the potential over snapshots extracted every 50 fs along the AIMD simulation, discarding the first 2–3 ps of the simulation for equilibration.

RESULTS

Structure and Electronic Properties of CFO Surfaces.

We considered two different cuts along orthogonal crystal planes in the CFO delafossite structure, reported in Figure S2: (i) the basal (0001) surface, shown in Figure S3a, corresponding to crystal growth along the [111] direction in rhombohedral coordinates (this orientation is reportedly accessible via templated epitaxial growth[16,51,52]), and (ii) the (11$\bar{2}$0) surface, shown in Figure S3b. This facet has been investigated in CFO nanocubes and nanoplates that are used as Fenton catalysts for the H_2O_2 activation step.[53] Slabs exposing the pristine (11$\bar{2}$0) surface are stoichiometric and non-polar, and they consist of linearly stacked $CuFeO_2$ units.

Figure 1a–f depicts three idealized terminations for the (0001) surface. The (0001) is a polar Tasker (III) surface, and consequently, adopting a symmetric slab with two identical terminations causes the loss of the Cu/Fe/O stoichiometric ratio within the unit cell. Among these three terminations, two have non-stoichiometric unit cells and are referred to as (0001) Fe/O (Figure 1f) and (0001) Cu (Figure 1d). The two non-stoichiometric surfaces can be considered as the Fe_xO_{2x} layer at zero and full Cu^+ coverage. The (0001) Fe/O surface is O-rich with no undercoordinated transition metal ions present. The (0001) Cu termination, having one undercoordinated Cu ion per surface oxygen, reconstructs to form dimers. We also considered the termination with half Cu coverage, which has an overall stoichiometric supercell, denoted as (0001) Cu_s (Figure 1e).

We investigated three different termination models based on the (11$\bar{2}$0) crystal plane, shown in Figure 1a–c. In general, the termination of the (11$\bar{2}$0) surfaces is unambiguously defined, given the equivalence of the layers. However, we considered also two defective surface models, which have overall non-stoichiometric unit cells. We denote as the (11$\bar{2}$0) Cu/O surface, Figure 1a, the system in which the outermost layers are completely Fe-depleted. In this case, all the cations are coordinated as in the bulk structure, while the oxygen ions in the two outermost layers are undercoordinated. In contrast, the surface Cu-depleted in the uppermost layer, the (11$\bar{2}$0) Fe/O system presented in Figure 1b, has dangling O-bonds exposed to the vacuum. In the pristine stoichiometric (11$\bar{2}$0),

https://dx.doi.org/10.1021/acscatal.0c05066
ACS Catal. 2021, 11, 1897−1910

which has no intrinsic vacancies, the O and Fe ions in the outermost layers have one and two dangling bonds, respectively.

On top of the described surfaces, we also considered the thermodynamic drive for the formation of surface point defects in the form of Fe, Cu, and O vacancies. As it has been reported for $LiCoO_2$,[54] which has the same $R\bar{3}m$ symmetry as CFO, O vacancies on top of the (0001) termination could help in stabilizing the surface through a vacancy-coupled charge redistribution.

The computed projected density of states (PDOS) for several of the (0001) surfaces is reported in Figure 2a–c. We

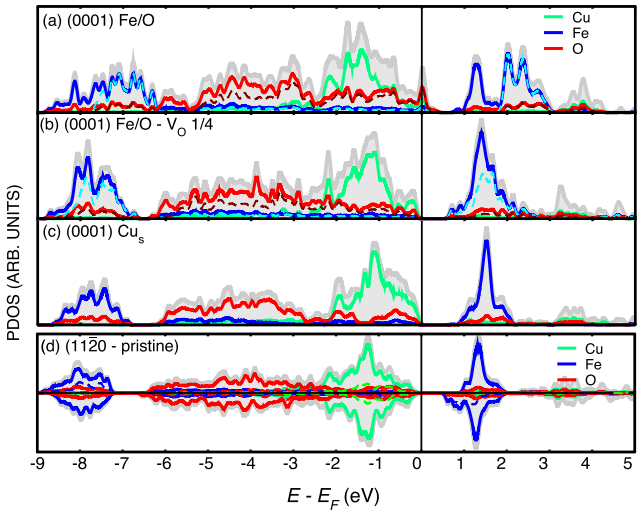

Figure 2. Projected density of states of the (0001) slab with the pristine Fe/O termination (a), the Fe/O termination with one 1/4 oxygen vacancies in the outermost layer (b), the stoichiometric Cu termination with 1/2 ML of Cu (c), and the pristine (11$\bar{2}$0) slab (d). The gray areas represent the total density of states. The dashed lines represent the density of states projected onto Fe/O atoms on the surface.

show the PDOS for a single spin polarization since each layer is composed of an equal number of Fe ions with opposite magnetization and the density of states is symmetric in the two spin channels. The (0001) Fe/O slab has a metallic behavior, showing a peak at the Fermi level with a prevalent O character. In particular, the brown dashed line in Figure 2a indicates that this peak is delocalized among the oxygen atoms in the outermost O–Fe–O layers. The Fe ions in the surface layer are still in their Fe^{3+} oxidation state, but the repulsion of the delocalized charge on the surrounding oxygen atoms pushes the energy of the states with an Fe d character ∼1 eV higher than the bulk-like counterpart, as shown by the light-blue dashed line in Figure 2.

The origin of the metallic character resides in the loss of the Cu/Fe/O stoichiometric ratio due to the symmetric construction of the slab. Two identical Fe/O cleavage planes lead to a globally Cu-deficient unit cell, and in a pure ionic picture, each missing Cu leaves the system with an excess hole. For a more detailed discussion on oxidation states, see the note in the Supporting Information. The redistribution of charge forming a metallic surface layer is a possible mechanism for stabilizing polar surfaces,[56] and it has been reported also for $LiCoO_2$,[54] which has the same $R\bar{3}m$ symmetry of CFO.

Conversely, an oxygen vacancy in the outermost layer could provide the charge that stabilizes the surface,[54] in particular when the excess charge due to the vacancy, formally 2 electrons per missing oxygen, compensates for the excess holes, provided that the Fe cations keep the Fe^{3+} oxidation state. This condition is achieved when 1/4 of the exposed oxygen atoms are removed. The corresponding slab loses the metallic character, restoring the semiconducting behavior as reported in Figure 2b. The compensation of the excess charges makes the electronic structure of the surface compatible with the bulk-like behavior. The peak at the Fermi level disappears, and the manifold of surface states with the Fe character overlaps with that of the bulk-like states. As we will show in the next section, this termination is energetically favored over the pristine metallic (0001) Fe/O termination.

Alternatively, the surface can be terminated with half a monolayer (ML) of Cu on both sides[54] as in the Cu_s termination to ensure a global neutrality of the slab and an equal charge distribution on the two facets; the PDOS of this configuration is reported in Figure 2c. It should be highlighted that polar surfaces can also be stabilized by the adsorption of quenching species:[56] the charge that compensates for the holes left by the lack of copper in the (0001) Fe/O surface can be provided not only by an oxygen vacancy but also by the addition of as many hydrogen atoms on the surface as the number of holes. Specifically, the undercoordinated oxygen atoms at the surface act as active sites for the adsorption of hydrogen atoms and the charge compensation is achieved when half of them are passivated.

The PDOS of the pristine (11$\bar{2}$0) surface is reported in Figure 2d. The projection onto the atoms in the outermost layers in which the Fe atoms have the majority-spin magnetization is indicated with dashed lines. The surface states differ from the bulk-like behavior especially in the lowest conduction states, which have an Fe d character. The surface states associated with the exposed Fe atoms form a peak that lies ∼0.4 eV lower in energy than the peak corresponding to the Fe in the central bulk-like layers due to the different coordination number of the external Fe. Conversely, the projection onto the wavefunctions of the exposed Cu and O atomic gives results that resemble the bulk-like behavior.

The PDOS of the Fe-depleted (Cu/O termination) and Cu-depleted (Fe/O termination) (11$\bar{2}$0) surfaces are reported in Figure S4. In both cases, the missing cations leave extra holes in the system, and these are delocalized among different surface atoms with the appearance of states at the Fermi level and just above. Further details of the geometry of different surface terminations are presented in Figures S2 and S3 in the Supporting Information.

Thermodynamic Stability in Vacuum: Surface Phase Diagram. In order to evaluate the thermodynamic stability of each surface, we have applied the ab initio thermodynamics formalism,[57,58] considering the surface to be in equilibrium with an oxygen atmosphere at fixed temperature and pressure. The relative thermodynamic stability of the different surfaces is assessed by comparing their surface free energies

$$\gamma = \frac{1}{2A}\left(G_{\text{slab}} - \sum_i N_i \mu_i\right) \quad (1)$$

where G is the Gibbs free energy of the slab, which is approximated with its DFT total energy, while μ_i and N_i represent the chemical potential and the number of atoms of

https://dx.doi.org/10.1021/acscatal.0c05066
ACS Catal. 2021, 11, 1897–1910

the ith species respectively, and the factor 2 takes into account that the surface is modeled by a slab with two identical terminations. The assumption of thermodynamic equilibrium in the bulk material introduces a constraint on the chemical potentials of the constituent species, $\mu_{Cu} + \mu_{Fe} + 2\mu_O = E^{bulk}_{CuFeO_2}$, with the consequence that only two of them are independent. The surface energies are usually reported either as a function of the chemical potential of oxygen for selected values of the chemical potential of one metallic species or in a 2D plot where the most stable termination is plotted as a function of two chemical potentials. Herein, we follow the approach of Jiang et al.,[59] plotting the surface with the lowest surface energy in a ternary plot to show explicitly the dependence on each chemical potential.

The phase diagram of CFO surfaces is reported in Figure 1 as a function of $\Delta\mu_i = \mu_i^{CFO} - \mu_i^{ref}$, which represents the difference between the chemical potential of the three species in CFO and in their bulk/gaseous reference phase. The derivation of the upper and lower bounds of each $\Delta\mu_i$ is reported in the Supporting Information.

Three different terminations are favored in the three limiting cases: when $\Delta\mu_{Fe}$ and $\Delta\mu_O$ are close to zero, the (0001) cut with the Fe/O termination represents the most stable surface and the stoichiometry of the employed slab ($Cu_4Fe_6O_{12}$) is consistent with the Cu-deficient conditions. A large portion of the diagram is dominated by this termination, which has a lower surface energy than the Cu-terminated (0001) surfaces, regardless of the chemical potentials. Based on earlier work, the relative instability of the Cu-terminated (0001) surfaces can be attributed to the fact that, despite surface reconstructions, the vacuum-exposed and uncoordinated Cu atoms yield significantly higher values of the surface energy.[60] In O-poor conditions, the O vacancies on the (0001) surface are thermodynamically stable and appear in the phase diagram in Figure 1. The density of the oxygen vacancies varies from 1/8 of the total exposed oxygen atoms to 1/4 going toward lower values of $\Delta\mu_O$. This last configuration is of particular interest since all the ions in the crystal are in their bulk oxidation state, as shown in the previous section.

The $(11\bar{2}0)$ surface is the most stable termination when $\Delta\mu_{Cu}$ is approaching zero. In Cu-rich conditions, the pristine $(11\bar{2}0)$ surface is the most favorable one for values of $\Delta\mu_{Fe}$ ranging from 0 to −3 eV. When $\Delta\mu_{Fe}$ becomes lower than −3 eV, iron vacancies on the surface begin to appear and the completely Fe-depleted $(11\bar{2}0)$ termination is the most stable one when $\Delta\mu_{Fe}$ is close to its lowest allowed value. In these Fe-deficient (Cu-rich) conditions, the Cu-based binary oxides are thermodynamically stable in the bulk phase diagram,[23] and this is reflected in the Fe-depleted termination of the slab ($Cu_{21}Fe_{15}O_{42}$).

The triangle in Figure 1 identifies the most stable termination in the range of all the allowed values for each $\Delta\mu_i$. A relevant subset of chemical potentials is the one that guarantees the stability of the underlying bulk delafossite CFO phase. We have recently determined the range of chemical potentials in which CFO is thermodynamically stable against the decomposition into other Cu- or Fe-based compounds.[23] The projection of the computed stability region of CFO into the ternary plot introduces further constraints, giving rise to the tiny region delimited by white lines in Figure 1.

Within this range of stability, the phase diagram in Figure 1 predicts that the pristine $(11\bar{2}0)$ surface has the lowest surface energy. However, we are not aware of a direct experimental characterization of this surface, possibly due to the incompatibility with the most commonly used substrates. The surface energies of the different terminations are reported in Table S1.

Thermodynamic Stability in an Electrochemical Environment: Surface Pourbaix Diagram. When in contact with an aqueous electrolyte, the surfaces are modified by (i) interactions with water molecules, which can adsorb molecularly or dissociatively, (ii) interactions with dissolved charged species, which create the electric double layer, and (iii) the possibility of electrochemical reactions taking place at the surface and leading to the formation of adsorbates or desorption of atoms from the oxide. In this work, we are interested in particular in the hydrogen evolution reaction, which can proceed through two mechanisms, namely, the Volmer−Tafel or the Volmer−Heyrovsky steps:

$$\text{Volmer step: } H^+_{aq} + e^- + \bigstar \rightarrow H^* \quad (2)$$

$$\text{Tafel step: } 2H^* \rightarrow H_{2,gas} + 2\bigstar \quad (3)$$

$$\text{Heyrovsky step: } H^* + H^+_{aq} + e^- \rightarrow H_{2,gas} + \bigstar \quad (4)$$

where ★ indicates an active site for adsorption and H* a hydrogen atom adsorbed on the active site. Regardless of which mechanism is kinetically favored, the first step consists of the discharge of a proton at the surface of the catalyst (Volmer step), leading to the adsorption of a hydrogen atom as an intermediate state in the HER. This step is influenced by the interaction with the adsorbates already present on the surface, giving rise to coverage-dependent adsorption free energies.[61] Therefore, the hydrogen coverage at specific electrochemical conditions depends on the thermodynamics of the Volmer step, which we evaluate via the computational hydrogen electrode (CHE) approach of Nørskov et al.[62]

Through the CHE, we constructed the surface Pourbaix diagram[63−68] of the CFO surfaces, showing the stability of different hydrogen coverage conditions as a function of the applied bias, measured with respect to the reversible hydrogen electrode, V_{RHE}. This term represents the electrochemical potential of the reservoir of electrons, and it will be initially treated as an independent variable, while later, we will consider how the band structure of CFO constrains the electrochemical potential of electrons in the dark and under illumination. The goal of this analysis is to predict the surfaces that are stable at values of the potential that correspond to dark and illuminated conditions. These representative surfaces will then be thoroughly characterized in the following sections.

We consider both the adsorption of H atoms and the formation of oxygen vacancies. The latter is the result of two H atoms adsorbing at the same oxygen site, leading to the desorption of a water molecule. We evaluate the formation energy of various structures as a function of the number of adsorbed H atoms, N_{H^*}, the number of oxygen vacancies, N_v, and V_{RHE}, according to

https://dx.doi.org/10.1021/acscatal.0c05066
ACS Catal. 2021, 11, 1897−1910

$$\Delta G(N_{H^*}, N_v, V_{RHE}) = G_{N_{H^*},N_v} - [G_{slab} + N_{H^*}(\mu_{e^-} + \mu_{H^+}) - N_v (\mu_{H_2O} - 2(\mu_{e^-} + \mu_{H^+}))] = G_{N_{H^*},N_v} - \left[G_{slab} + (N_{H^*} + 2N_v)\frac{\mu_{H_2}}{2} - N_v\mu_{H_2O}\right] - (N_{H^*} + 2N_v)eV_{RHE} = \Delta G^{form}_{N_{H^*},N_v} - (N_{H^*} + 2N_v)eV_{RHE} \quad (5)$$

where we used the fact that $\mu_{e^-} + \mu_{H^+} = 1/2\mu_{H_2} + eV_{SHE} - RT$ ln 10 × pH where the free energy of the H_2 molecule is evaluated at standard conditions, T = 298.15 K and p = 1 bar; moreover, $V_{RHE} = V_{SHE} - RT$ ln 10/e × pH. The subscripts "slab" and N_{H^*}, N_v refer to the pristine slab and the slab with N_{H^*} adsorbed hydrogen atoms and N_v oxygen vacancies, respectively. The free energy of formation $\Delta G^{form}_{N_{H^*},N_V}$ is computed as

$$\Delta G^{form}_{N_{H^*},N_v} = \Delta E^{form}_{N_{H^*},N_v} + \Delta E_{ZPE} - T\Delta S \quad (6)$$

where $T\Delta S$ and ΔE_{ZPE} are the energy changes due to entropic and zero-point effects and $\Delta E^{form}_{N_{H^*},N_V}$ is the DFT formation energy. A possible limitation of this model resides in the fact that we computed the formation free energies $\Delta E^{form}_{N_{H^*},N_V}$ in vacuum in the absence of any explicit or implicit solvent, thus neglecting solvation effects.

The surface Pourbaix diagrams of the (0001) and the (11$\bar{2}$0) surfaces are shown in Figure 3, while the list of the employed

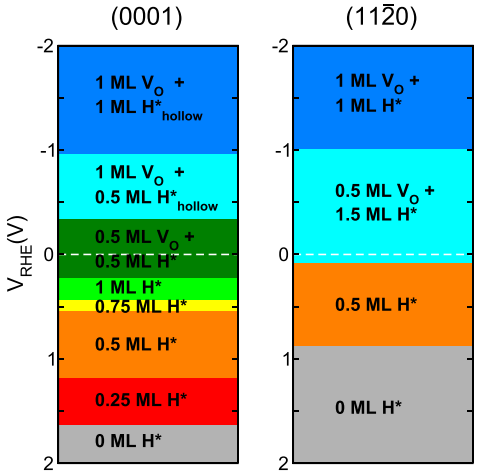

Figure 3. Surface Pourbaix diagram of the CFO(0001) (left) and CFO (11$\bar{2}$0) (right) surfaces, showing the potential-dependent surface coverage.

reactions and the associated free energies of adsorption are reported in Tables S2 and S3. On the pristine (0001) surface with the Fe/O termination, the outermost oxygen atoms are the only active sites for hydrogen adsorption. Each value of the coverage is related to the total number of surface oxygen sites of the pristine surface, and wherever not explicitly indicated, H* refers to the absorption of a hydrogen atom on an oxygen site. We first considered the case of 0, 1/4, 1/2, 3/4, and 1 ML of hydrogen coverage. When the coverage of the H* is less than 0.5 ML, the hydrogen atoms supply the missing charge due to the Cu deficiency of the slab, saturating all the holes at half H* coverage conditions. Further, hydrogen atoms added on the surface reduce Fe^{3+} ions on the outermost layer to Fe^{2+}. The threshold at which the reduction processes begin to take place is 0.54 V versus RHE, corresponding to the transition between 0.5 ML H* (orange area) and 0.75 ML H* (yellow area). This value compares favorably with a recent measurement in which a polaronic Fe^{3+}/Fe^{2+} charge transition level has been observed at 0.7 V versus RHE, inducing Fermi level pinning and limiting the performance of CFO as a photocathode.[20] The presence of a state inducing Fermi level pinning at this potential was previously reported and attributed to the formation of a surface metal hydroxide.[11]

Further increasing the surface hydrogenation leads to the formation of O vacancies. When two H atoms adsorb on the same oxygen site, a water molecule forms at the active site and desorbs leading to a surface O vacancy. For this reason, we investigated different coverages of oxygen vacancies, ranging from a single vacancy in a large supercell to the full oxygen depletion in the outermost layer. Moreover, additional hydrogen atoms can be adsorbed on the hollow sites formed by oxygen vacancies with a bond length of ∼2 Å with the three surrounding Fe ions. This configuration is more favorable than the absorption on top of undercoordinated Fe sites or in a bridging position between two sites. The top view of these structures is reported in Figure S5.

When a hydrogen atom is nearby a surface already containing oxygen vacancies, there is competition between the creation of a new vacancy or the adsorption on a hollow site. In the former case, the entropic contribution of desorbed water molecules becomes significant in the Gibbs free energy, while the latter entails a gain in the enthalpic term. The upper part of the Pourbaix diagram reveals that a high density of oxygen vacancies from 0.5 to 1 ML is expected on the surface for negative values of V_{RHE}, while the adsorption of hydrogen atoms on hollow sites is thermodynamically stable for a V_{RHE} more negative than −0.34 V. In contrast with the adsorption of H* on the oxygen sites in which the thermodynamically stable structures show an increasing coverage, there is a net transition between the configuration with 0.5 ML H* + 0.5 ML V_O (dark green) and that with 1 ML V_O + 0.5 ML H^*_{hollow} (cyan).

The (11$\bar{2}$0) surface exposes undercoordinated Fe and O atoms that may host the hydrogen adsorption. However, the binding energy is extremely different in the two cases. While hydrogen atoms are strongly bound when adsorbed to the oxygen sites, ΔG^{ads}_H = − 1.25 eV, the adsorption on Fe sites is highly unfavored, ΔG^{ads}_H = 0.78 eV. For this reason, we investigated the relative stability of adsorption on oxygen atoms only with coverages of 0 ML, 1/3 ML, 1/2 ML, 2/3 ML and 1 ML H*. In analogy with the (0001) termination, we investigated the formation of oxygen vacancies at the surface after complete hydrogenation of the oxygen sites.

Only four phases are thermodynamically stable in the surface Pourbaix diagram of CFO (11$\bar{2}$0). First, the pristine surface is the most stable configuration for a V_{RHE} more positive than 0.87 V. The surface with 0.5 ML H* occupies the portion between 0.87 and 0 V. Among the different ways to adsorb on half of the oxygen sites, the configuration with the lowest energy is the one with an alternate arrangement in such a way that the hydroxyls have the maximum possible distance among them, hence the lowest repulsion. At half-coverage conditions, the Fe ions in the outermost layer are completely reduced to Fe^{2+}.

https://dx.doi.org/10.1021/acscatal.0c05066
ACS Catal. 2021, 11, 1897−1910

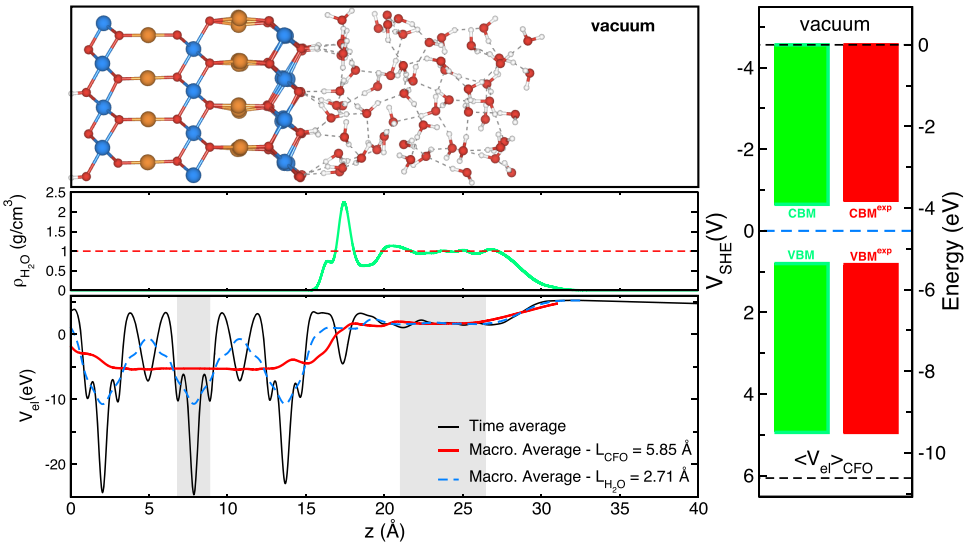

Figure 4. Interface between the (0001) surface and water (top panel), water density profile (middle panel), and electrostatic potential across the interface (bottom panel). The gray areas indicate the regions from which we extracted the average electrostatic potential of CFO and water. Alignment of the band edges w.r.t. SHE and comparison with the experimental data of Prévot et al.[7] (right panel).

For negative values of V_{RHE}, the thermodynamically stable phases contain oxygen vacancies. When a single oxygen vacancy is created, one subsurface oxygen atom breaks an O−Fe bond and migrates toward the surface. A second hydrogen atom can now be adsorbed either on this oxygen site or in a bridging position between the undercoordinated cations. Alternatively, it can create a second oxygen vacancy by absorbing on another hydroxyl group. According to the free energies reported in Table S2, the adsorption at a bridging site between undercoordinated Cu and Fe ions is favored for a low density of oxygen vacancies, where there is a negligible interaction among them. However, this configuration is not a thermodynamically stable phase in the Pourbaix diagram. Indeed, the most stable surface between 0 and −1 V, shown in Figure S7d and corresponding to the turquoise area in Figure 3, has a higher density (0.5 ML) of oxygen vacancies on the surface. In this configuration, the cations on the surface move toward the second layer, forming a single Cu- and Fe-rich layer in which the subsurface oxygen atoms are now exposed to the vacuum and host the hydrogen adsorption. For such a significant density, the adsorption on bridging sites is no longer energetically relevant. Above 1 V, an additional 0.5 ML of hydrogen atoms is adsorbed on the hydroxyl groups formed by the oxygen sites that were originally present on the surface, forming water molecules that desorb from the surface.

Band Alignment in Dark Conditions. When the electrode is not illuminated (dark conditions) and at flatband conditions, the Fermi level of the semiconductor corresponds to the flatband potential, which is approximately equal to 1 V (RHE) for CFO.[7] The computed thermodynamics predicts that, at this bias, the most stable phases in the Pourbaix diagram are the pristine (11$\bar{2}$0) and the surface with 0.5 ML H* for the (0001). In both cases, all the atoms are in the same oxidation state as in the bulk. In this section, we describe the alignment of the band edges of these two surfaces in the dark.

Band Alignment of the (0001) Surface. We performed the AIMD simulation of the (0001) surface with 0.5 ML of adsorbed hydrogen atoms in contact with a 15 Å thick slab of water, fixing the bottom three layers. The side view of the interface is reported in the top panel of Figure 4. In the middle panel of Figure 4, we show the average density distribution of water molecules as a function of the position z in the direction perpendicular to the surface. Two different regions are easily distinguished: a first peak, corresponding to a layer of water molecules accumulated close to the CFO surface, and a bulk-like region in which the density of water oscillates around 1 g/cm^3. In hydroxylated surfaces in contact with water, the formation of an interfacial layer with higher density than bulk water has been observed.[43,69,70] In this interfacial layer, whose thickness is ∼3 Å, the water molecules form an extended network of hydrogen bonds with the undercoordinated oxygen atoms of the substrates. In Figure S11, we report the distribution of water molecule orientations, the main peak corresponds to water molecules within the interfacial layer, donating hydrogen bonds to the oxygen atoms of the surface.

The time average of the electrostatic potential profile is shown in the bottom panel of Figure 4. We performed a macroscopic average of the potential profile to compute the potential drop at the CFO−water interface.[71,72] The macroscopic average was computed with two different periods to reduce the oscillations in the CFO or water side of the interface. The red curve represents the macroscopic average with a period of 5.85 Å, equal to the periodicity of the CFO slab in the z direction. The period of the blue dashed line, 2.71 Å, corresponds to the peak of the O−O radial distribution function of bulk water. We computed the potential drop across the interface as the difference between the average of the red curve in the center of the slab and the average of the blue one in the bulk-like region of water, as indicated by the gray areas in Figure 4, obtaining a value of 6.92 ± 0.02 eV.

In the right panel of Figure 4, we report the band alignment following the approach outlined in the Computational Methods section. Our predicted values for the conduction band maximum (CBM) and valence band minimum (VBM) are −0.65 ± 0.02 V and +0.82 ± 0.02 V versus SHE. To make a direct comparison with the experimental data, we should keep in mind that the AIMD simulations are equivalent to experiments performed at the pH corresponding to the point of zero charge (PZC). According to the PEC measurements of Prévot et al.[7] performed in alkaline conditions at pH = 13.6,

https://dx.doi.org/10.1021/acscatal.0c05066
ACS Catal. 2021, 11, 1897−1910

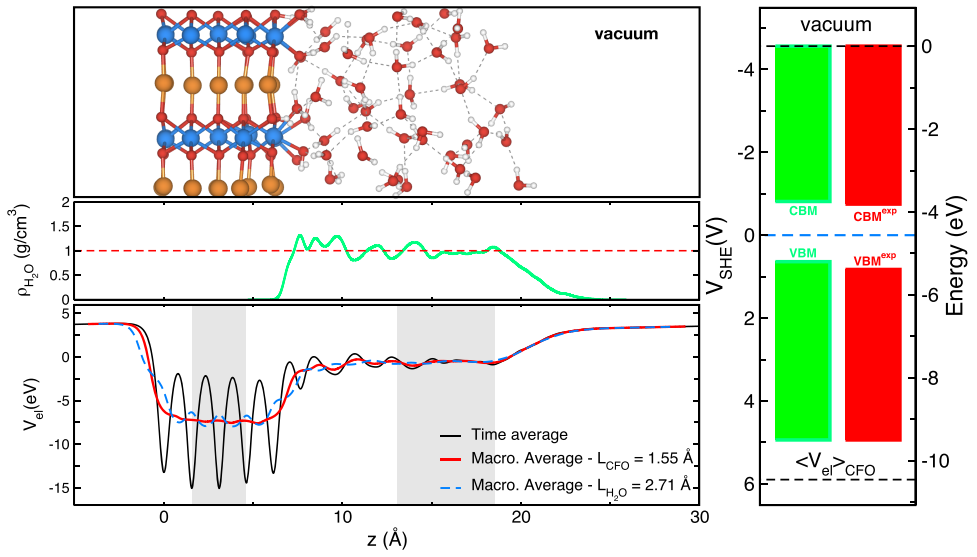

Figure 5. Interface between the $(11\bar{2}0)$ surface and water with one water molecule initially dissociated on each Fe site (top panel). Water density profile (middle panel) and electrostatic potential across the interface (bottom panel). The gray areas indicate the regions from which we extracted the average electrostatic potential of CFO and water. Alignment of the band edges w.r.t. SHE and comparison with the experimental data of Prévot et al.[7] (right panel).

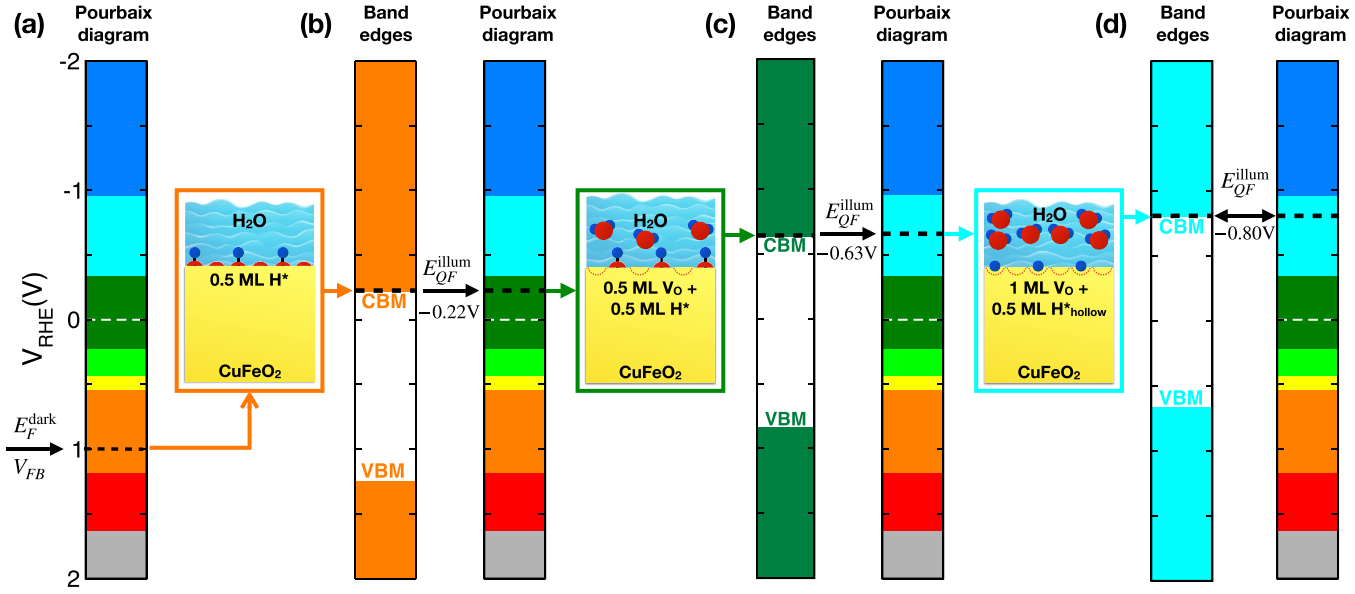

Figure 6. Steps of the procedure employed to predict the most stable coverage under illumination based on the self-consistency between the position of the CBM of a specific surface structure and the stability region of the structure in the Pourbaix diagram. The band edges are reported with the same color as the corresponding structure in the Pourbaix diagram.

the CBM and VBM of CFO at flatband conditions lie at −0.32 V and +1.26 V versus the reversible hydrogen electrode (RHE), respectively. Assuming that the bands have a Nernstian dependence on the pH,[73,74] $V_{SHE}(pH_{PZC}) = V_{SHE}(pH) - (0.059\ V) \times (pH_{PZC} - pH)$, and using the experimental estimate of the PZC, pH_{PZC} =7.36,[15] the resulting experimental band edges depicted with the red dashed lines in Figure 4 lie at −0.75 V and +0.83 V versus SHE. Our VBM is in excellent agreement with the experimental value, while the position of the CBM is slightly underestimated. This is due to the fact that the gap is slightly underestimated within the approach adopted to describe the electronic structure of bulk CFO.

Band Alignment of the $(11\bar{2}0)$ Surface. The pristine surface is the thermodynamically stable phase of the $(11\bar{2}0)$ termination of CFO in dark conditions at the flatband potential. When this termination is exposed to liquid water, our AIMD simulations show that the first layer of water is absorbed in a mixed mode where half the water molecules are adsorbed molecularly and half are dissociated (see the Supporting Information and Figure S10).

The water density profile, reported in the middle panel of Figure 5, shows a region close to the surface with three peaks at a slightly higher density than bulk water. This feature is due to the fact that water molecules adsorb only on top of surface Fe sites, creating vacuum pockets around the hydrophobic Cu sites. As shown in Figure S12, the water molecules close to the

https://dx.doi.org/10.1021/acscatal.0c05066
ACS Catal. 2021, 11, 1897−1910

surface arrange themselves with the hydrogen atoms pointing upward, bringing a dipole moment opposite to that of the (0001). Conversely, the majority of the OH groups of the dissociated molecules are arranged with the hydrogen atoms directed toward the surface.

We found an electrostatic potential difference across the interface of 6.77 ± 0.03 eV, which is 0.15 eV lower than the value obtained for the (0001) surface. Consequently, the band alignment reported in the right panel of Figure 5 provides values of the VBM and the CBM 0.15 eV higher than on the (0001) surface, namely, at +0.67 ± 0.03 V and −0.80 ± 0.02 V versus SHE, respectively.

If CFO particles expose different facets, this difference in the position of the band edges could result in an anisotropic charge separation with the photogenerated electrons migrating toward the surface with a lower CBM. It has been reported that, in $SiTiO_3$, a gradient bigger than 0.1 eV in the workfunction between two different facets is sufficient to drive an anisotropic charge separation.[75] If all or part of the difference in band edge alignment between the two facets results in a potential drop inside the semiconductor rather than in the electrolyte, then the resulting electric field within CFO will force photoexcited electrons toward the (0001) termination, discouraging the $(11\bar{2}0)$, in analogy with Ta $_3N_5$. For this reason, in the following section where we examine the effects of illumination, we will focus mainly on the (0001) surface.

Band Alignment under Illumination. After the investigation of CFO surfaces in contact with water in dark conditions, the aim of this section is to predict the surface structures that might form under illumination. To this end, we introduce a simple thermodynamic model to link the stable phases in the Pourbaix diagram with the electrochemical potential of the electrons under illumination, which is schematically reproduced in Figure 6.

When photo-excited electrons driven by band bending at the solid/liquid interface reach the surface, we assume that their electrochemical potential, i.e., the electron quasi-Fermi level E_{QF}^{illum}, corresponds to the potential of the CBM edge at the interface with the electrolyte. The thermodynamic driving force for water reduction is therefore given by the position of the CBM edge,[76] while we neglect processes that might take place through the valence band.

If the CBM of a surface structure is sufficiently high in energy to make the discharge of protons ($H^+ + e^- \rightarrow H^*$) energetically downhill, light absorption can induce hydrogen adsorption, leading to the formation of a new surface structure. On the basis of these assumptions, the surface structure that forms for a given position of the CBM can be determined from the Pourbaix diagram by equating the electrochemical potential of electrons to the CBM. We report in Figure 6 the scheme of this procedure, showing the band edges of selected phases of the Pourbaix diagram of the (0001) surface computed following the method outlined in the previous section and reproduced using the same color code as in the Pourbaix diagram.

As we have already pointed out, the Fermi level in dark conditions E_F^{dark} is equivalent to the flatband potential of CFO, which lies at 1 V versus RHE. At this potential, the most stable termination in the Pourbaix diagram is the one with half coverage of H* (orange area in Figure 6a). The CBM of this surface in dark conditions lies at −0.22 V versus RHE (Figure 6(b)), photo-excited electrons reaching the solid/liquid interface will therefore have a quasi-Fermi level E_{QF}^{illum}, hence an electrochemical potential of −0.22 V. At this potential, the stable surface structure is the one containing 0.5 ML of oxygen vacancies and 0.5 ML of adsorbed hydrogen (dark green area in the Pourbaix diagram). Light absorption will therefore drive the transition from the surface that is stable in the dark conditions (orange) to a partially reduced surface (dark green). However, as shown in Figure 6c, the CBM of this surface lies at −0.63 V (dark green), which is in the region of stability for the surface containing 1.0 ML of oxygen vacancies and 0.5 ML of hydrogen adsorbed in hollow sites within those vacancies (cyan). Our simulations predict that light absorption will drive a further reduction from the dark green to the cyan surface. The CBM of the latter is at −0.80 V (cyan in Figure 6d) and lies within the region of stability of the cyan surface itself. At this point, there is no further driving force for illumination-mediated reduction of the surface, and we have reached self-consistency between the position of the CBM of a surface structure and its region of stability as determined from the Pourbaix diagram.

Clearly this model, based on thermodynamics considerations, neglects any kinetic component, which may play a fundamental role in the adsorption processes, possibly inhibiting some transitions. Moreover, our assumption that the electron quasi-Fermi level coincides with the CBM should be validated against a full kinetic model that includes the rates of all relevant process (e.g., generation of photocarriers, recombination in the bulk and at the surface, diffusion, and surface reaction) to obtain the steady-state concentration of photoexcited electrons at the solid−liquid interface. Steps in this direction have been recently taken by Iqbal and Bevan.[77]

The key finding of our analysis is that the thermodynamically stable surface under illumination predicted by this model differs from the surface in dark conditions by the presence of 1 ML of oxygen vacancies and the adsorption of hydrogen atoms in these vacancy sites (hollow sites with respect to the three surrounding Fe atoms). The main difference between the hydrogen atoms in the hydroxyl groups and in the hollow sites resides in their charge state. While the Bader/Löwdin electronic charge of the hydrogen atoms in hydroxyls is 0.34/0.60 e (H^+), the charge of the hydrogen in the hollow sites is 1.52/1.46 e, indicating that the latter are negatively charged hydride species (H^-). Interestingly, hydride species formed at oxygen vacancies were predicted theoretically and observed experimentally as HER intermediates on Rh-doped TiO_2[78] with values of the Bader charge on H^- as 1.34 e, in line with our results. The formation of negatively charged hydrogen adsorbates is particularly intriguing since hydride species could lead to facile H_2 production, reacting with a proton in solution ($H^- + H^+ \rightarrow H_2$).

Moreover, the proton discharge and the formation of oxygen vacancies leads to the reduction of the surface, resulting in the conversion of all the Fe ions in the first layers to Fe^{2+}. This process introduces filled states in the gap, as shown by the PDOS displayed in Figure 7.

We found the presence of mid-gap states with Fe characters of 0.8 and 0.5 eV above the bulk VBM level for the surface with 1 ML H* and 1 ML V_O and 0.5 ML H^*_{hollow}, respectively, in good agreement with experimental evidence. These states might explain the origin of the light-induced Fermi-level pinning observed in recent experiments on CFO.[11] Prévot et al.[11] observed surface states at ∼0.4 eV above the valence band edge, which are detrimental to the performance of CFO as a photocathode since they limit the photovoltage. Our results

https://dx.doi.org/10.1021/acscatal.0c05066
ACS Catal. 2021, 11, 1897−1910

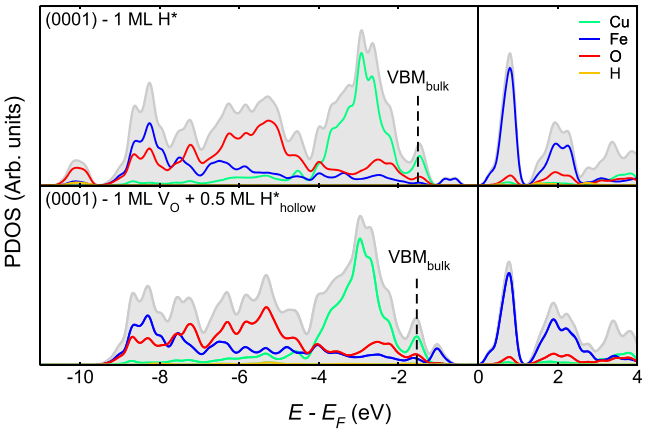

Figure 7. Projected density of states of the (0001) slab with 1 ML of H* coverage (top panel) and 1 ML of oxygen vacancies and 0.5 ML of hydrogen adsorbed at hollow sites (bottom panel), performed with the hybrid PBE0 exchange-correlation functional. The VBM of the bulk phase is indicated by dashed lines.

offer a possible explanation for the formation of these states under illumination.

While the XPS measurements reported did not detect the presence of Fe^{2+} states, we stress that, according to our work, these states are formed under illumination and in the presence of the electrolyte. Consequently, it is unlikely that they could be detected in ex situ measurements such as those of Prévot et al.[11]

In our analysis of the thermodynamic stability of surface structures under illumination, we have considered only reduction processes taking place at the surface, such as hydrogen adsorption and the formation of oxygen vacancies. Our previous work on bulk Cu/Fe/O systems,[23] however, shows that the region of stability of CFO against reduction to metallic Cu is narrow with the transition to Cu^0 taking place at potentials within the band gap of CFO. Under illumination, CFO should therefore be photoreduced to metallic Cu, similar to the case of Cu_2O.[5] CFO, however, is credited with stability under operation extending to days,[11] even though signatures for the presence of metallic Cu have been detected in experiments extending to several hours.[79] This suggests that either kinetic factors[76] or the formation of metastable surface structures that are difficult to reduce further, like the one we determined on the (0001) facet under illumination, govern the stability of CFO with respect to photocorrosion.

Incremental Gibbs Free Energy of Adsorption of Atomic Hydrogen. A good descriptor for the catalytic activity of an electrode for HER is the incremental Gibbs free energy for hydrogen adsorption

$$\Delta G^{\mathrm{incr}}_{\mathrm{H}^*} = G_{\mathrm{slab}+(N+1)_{\mathrm{H}}} - \left(G_{\mathrm{slab}+N_{\mathrm{H}}} + \frac{1}{2}G_{\mathrm{H}_2,\mathrm{mol}}\right) \quad (7)$$

which provides a measure of the energy cost/gain to add one extra hydrogen adsorbate to the surface. In a metallic electrode at zero potential with respect to RHE, the initial state ($H^+ + e^-$) and the final state ($\frac{1}{2}H_2$) are in equilibrium, and an optimal catalyst promotes the reaction via intermediate states with $\Delta G^{\mathrm{incr}}_{\mathrm{H}^*} \approx 0$[80] to avoid "thermodynamic barriers" for the adsorption or desorption process. The catalytic activity plotted as a function of the binding energy gives rise to the well-known volcano plot in which platinum lies on top with $\Delta G^{\mathrm{incr}}_{H^*} \approx 0$ and the highest activity.[81−83]

In a semiconducting photoelectrode, the free energy of the initial state in which the electron lies at the conduction band is higher than the one of the final state by a quantity of eV_{CBM}(RHE). In this case, a good photocatalysts is the one that creates an intermediate state whose incremental free energy lies between the potential of the conduction band and zero so that no thermodynamic barriers are created neither for adsorption of H* nor for desorption of H_2.

We computed the incremental free energies $\Delta G^{\mathrm{incr}}_{\mathrm{H}^*}$ by adding one hydrogen atom to the stable phases of the Pourbaix diagram of the (0001) surface, and the resulting values are used to construct the free energy diagram in Figure S18. The free energy diagram for the most stable surfaces in the dark and under illumination is shown in Figure 8. The reaction

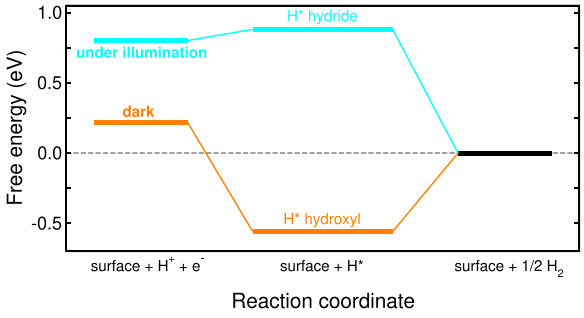

Figure 8. Free-energy diagram for hydrogen evolution on the CFO(0001) surface in the dark and under illumination. The free energy of the final state is set to zero in both cases. The color code is the same as in Figure 3, namely, 0.5 ML H* (orange), 0.5 ML H_{hollow} + 1 ML V_O (cyan).

coordinate describes the energetics of the proton discharge (Volmer step) followed by the desorption of molecular hydrogen. In the initial state, we considered a proton in solution and an electron lying in the CBM of the structures computed in the previous section, which are reported with the same color code as in Figure 3. In the intermediate state, an additional hydrogen atom is adsorbed on the surface with a corresponding variation in coverage of 0.06 ML. We set the free energies of the final state of each configuration to zero so that the free energy of the intermediate state is $\Delta G^{\mathrm{incr}}_{\mathrm{H}^*}$, according to eq 7, while the free energy of the initial state, if present, is eV_{CBM}(RHE).

When the H* coverage of the intermediates on the (0001) surface is lower than 0.5 ML, there is a large barrier for hydrogen desorption due to the strong O−H bond, indicating that the low-coverage configurations are not effective for the hydrogen production. In particular, $\Delta G^{\mathrm{incr}}_{\mathrm{H}^*}$ in half-coverage conditions is about −1 eV for the (0001) surface and even lower for lower H* coverage.

In half-coverage conditions, hydrogen atoms are adsorbed at second nearest neighbor sites; an additional hydrogen atom will introduce nearest neighbor repulsive interactions, reducing its binding strength. Moreover, the addition of a hydrogen atom causes the reduction of a surface Fe^{3+} to Fe^{2+}. As a result, there is a variation of ∼0.5 eV in $\Delta G^{\mathrm{incr}}_{\mathrm{H}^*}$ when the H* coverage of the intermediates changes from 0.5 ML to 0.56 ML.

The orange path in Figure 8 represents the free energy path of the HER on the (0001) surface, starting from half-coverage conditions. The proton discharge is energetically favorable

https://dx.doi.org/10.1021/acscatal.0c05066
ACS Catal. 2021, 11, 1897−1910

with a free energy variation of −0.77 eV, yet the hydrogen desorption is still the limiting step with a free energy cost of 0.55 eV. The hydrogen in the surface hydroxyl groups are therefore bound too strongly, thus introducing a sizable barrier for desorption of H_2 on the (0001) surface. Conversely, the hydrogen atoms in the hydride species at the hollow sites show better catalytic activity, according to the $\Delta G^{incr}_{H^*}$ descriptor. The proton discharge on a hollow site on the surface with 1 ML V_O and 0.5 ML H^*_{hollow} (cyan path) exhibits a free energy cost of 0.1 eV and a favorable desorption free energy of −0.88 eV.

These results show that hydrogen atoms in the hydride state introduce very small thermodynamic barriers for adsorption. The fact that these species, present in thermodynamically stable surface under illumination (1 ML V_O and 0.5 ML H^*_{hollow}), have favorable adsorption energy is encouraging for using CFO as a photocathode. Moreover, this suggests that the catalytic step of HER might not be the culprit for the poor performance of CFO as a photocatalyst.

The incremental Gibbs free energy of adsorption of hydrogen on the $(11\bar{2}0)$ surface is reported in Figure S16. In this case, the H* on the hydroxyl groups are less bound than in the (0001) and may be catalytically active.

A possible limitation of our analysis is the fact that we have considered the CBM as the electrochemical potential of the photogenerated electrons. In the presence of polaronic or defect states within the energy gap, the photoexcited electrons may be trapped in these states rather than in the CBM, thus providing a lower overpotential to drive the HER. Polaronic states originating from Fe^{3+}/Fe^{2+} reduction have been suggested as limiting factors in CFO,[20] leading to Fermi-level pinning in the bulk. In this case, the photovoltage would be lower compared to the one estimated from the position of the CBM and the band bending would be reduced, hindering charge carrier separation.

Moreover, the incremental free energies were calculated by removing a hydrogen atom from the surface exposed to the vacuum, thus neglecting the effect of the solvent. Although it is common to use the free energy differences computed in vacuum,[84] the solvent could have a small but non-negligible effect on the calculation of the adsorption energies.[85]

CONCLUSIONS

We investigated the (0001) and $(11\bar{2}0)$ facets of CFO, considering different terminations and evaluating the phase diagram in vacuum, identifying the surfaces with the lowest formation energy within the limits imposed by the stability of the bulk phase. Among them, the pristine $(11\bar{2}0)$ and a Fe/O terminated (0001) surfaces represent our best candidates for modeling CFO as a photoelectrode in vacuum.

To model the CFO surfaces in an electrochemical environment, we investigated the interaction of various terminations with the electrolyte, considering both the proton discharge leading to hydrogen adsorption and the formation of oxygen vacancies. From the surface Pourbaix diagrams, we inferred the most stable terminations in dark conditions at the flatband potential. To predict the position of the band edges of CFO on the electrochemical scale, we modeled these surfaces in contact with water using ab initio molecular dynamics, simulating water explicitly. We obtained for both the (0001) and $(11\bar{2}0)$ surfaces results in line with the experimental measurements, suggesting that the surface terminations predicted in this work are a reliable model of the surface structures of CFO in contact with the electrolyte.

To model the system under illumination, we looked for self-consistency between the CBM of a specific structure and the stability of the structure in the Pourbaix diagram at the potential given by its CBM. We found that the illumination changes the adsorption state on the surface. While the (0001) surface in dark conditions shows half-coverage of hydroxyl groups, we predict the formation of oxygen vacancies and the adsorption of hydride species at these vacancies under illumination. In this surface structure, all the Fe ions in the first layer, directly in contact with the electrolyte, are reduced from Fe^{3+} to Fe^{2+}, giving rise to states in the gap that can pin the Fermi level. Measurements able to detect these changes in the oxidation state, such as operando core-level X-ray spectroscopy, would be instrumental in validating our findings. Hydrides were detected on Rh-doped TiO_2 using vibrational spectroscopy,[78] suggesting that this technique could be applicable to CFO too.

The illumination affects also the catalytic activity of the surface. Indeed, using the adsorption energy of hydrogen as a descriptor of the catalytic activity, we found that, in the (0001) surface, the hydrogen atoms in the hydroxyl groups are bound very strongly, hence the formation of molecular hydrogen via these species would involve a large kinetic barrier. Hydride atoms formed in the hollow sites created by oxygen vacancies, on the other hand, have a near optimal adsorption energy and would afford favorable kinetics with only a small thermodynamic barrier for adsorption.

ASSOCIATED CONTENT

Supporting Information

The Supporting Information is available free of charge at https://pubs.acs.org/doi/10.1021/acscatal.0c05066.

Construction and the structural properties on the surfaces, ab initio thermodynamic formalism, adsorption reactions and free energies employed to construct the surface Pourbaix diagrams, CFO−water interface models and water orientation at the interface, band alignment procedure, $(11\bar{2}0)$ surface under illumination and relative incremental Gibbs free energy, and additional references not present in the main text[86−94] (PDF)

AUTHOR INFORMATION

Corresponding Author

Simone Piccinin − *CNR-IOM, Consiglio Nazionale delle Ricerche - Istituto Officina dei Materiali, c/o SISSA, 34136 Trieste, Italy;* orcid.org/0000-0002-3601-7141; Email: piccinin@iom.cnr.it

Authors

Matteo Ferri − *International School for Advanced Studies (SISSA), I-34136 Trieste, Italy;* orcid.org/0000-0002-4768-8012

Joshua David Elliott − *CNR-IOM, Consiglio Nazionale delle Ricerche - Istituto Officina dei Materiali, c/o SISSA, 34136 Trieste, Italy;* orcid.org/0000-0002-0729-246X

Matteo Farnesi Camellone − *CNR-IOM, Consiglio Nazionale delle Ricerche - Istituto Officina dei Materiali, c/o SISSA, 34136 Trieste, Italy;* orcid.org/0000-0001-9180-0115

Stefano Fabris − *CNR-IOM, Consiglio Nazionale delle Ricerche - Istituto Officina dei Materiali, c/o SISSA, 34136 Trieste, Italy;* orcid.org/0000-0003-2562-8788

https://dx.doi.org/10.1021/acscatal.0c05066
ACS Catal. 2021, 11, 1897−1910

Complete contact information is available at: https://pubs.acs.org/10.1021/acscatal.0c05066

Author Contributions

[§]M.F. and J.D.E. contributed equally to this work.

Notes

The authors declare no competing financial interest.

■ ACKNOWLEDGMENTS

We acknowledge the CINECA award under the ISCRA initiative for the availability of high-performance computing resources and support. Most of the calculations of this work were performed on Marconi KNL and Marconi100 under the ISCRA B project CUPHERO.

■ REFERENCES

(1) Hisatomi, T.; Kubota, J.; Domen, K. Recent Advances in Semiconductors for Photocatalytic and Photoelectrochemical Water Splitting. *Chem. Soc. Rev.* **2014**, *43*, 7520−7535.
(2) Brahms, S.; Nikitine, S.; Dahl, J. P. On the Band Structure and the Absorption Spectrum of Cu_2O. *Phys. Lett.* **1966**, *22*, 31−33.
(3) Hara, M.; Kondo, T.; Komoda, M.; Ikeda, S.; Kondo, J. N.; Domen, K.; Hara, M.; Shinohara, K.; Tanaka, A. Cu_2O as a Photocatalyst for Overall Water Splitting under Visible Light Irradiation. *Chem. Commun.* **1998**, 357−358.
(4) de Jongh, P. E.; Vanmaekelbergh, D.; Kelly, J. J. Cu_2O: a Catalyst for the Photochemical Decomposition of Water? *Chem. Commun.* **1999**, 1069−1070.
(5) Paracchino, A.; Laporte, V.; Sivula, K.; Grätzel, M.; Thimsen, E. Highly Active Oxide Photocathode for Photoelectrochemical Water Reduction. *Nat. Mater.* **2011**, *10*, 456−461.
(6) Read, C. G.; Park, Y.; Choi, K.-S. Electrochemical Synthesis of p-Type $CuFeO_2$ Electrodes for Use in a Photoelectrochemical Cell. *J. Phys. Chem. Lett.* **2012**, *3*, 1872−1876.
(7) Prévot, M. S.; Guijarro, N.; Sivula, K. Enhancing the Performance of a Robust Sol-Gel-Processed p-Type Delafossite $CuFeO_2$ Photocathode for Solar Water Reduction. *ChemSusChem* **2015**, *8*, 1359−1367.
(8) Jang, Y. J.; Park, Y. B.; Kim, H. E.; Choi, Y. H.; Choi, S. H.; Lee, J. S. Oxygen-Intercalated $CuFeO_2$ Photocathode Fabricated by Hybrid Microwave Annealing for Efficient Solar Hydrogen Production. *Chem. Mater.* **2016**, *28*, 6054−6061.
(9) Prévot, M. S.; Li, Y.; Guijarro, N.; Sivula, K. Improving Charge Collection with Delafossite Photocathodes: a Host-guest $CuAlO_2$/$CuFeO_2$ Approach. *J. Mater. Chem. A* **2016**, *4*, 3018−3026.
(10) Oh, Y.; Yang, W.; Kim, J.; Jeong, S.; Moon, J. Enhanced Photocurrent of Transparent $CuFeO_2$ Photocathodes by Self-Light-Harvesting Architecture. *ACS Appl. Mater. Interfaces* **2017**, *9*, 14078−14087.
(11) Prévot, M. S.; Jeanbourquin, X. A.; Bourée, W. S.; Abdi, F.; Friedrich, D.; van de Krol, R.; Guijarro, N.; Le Formal, F.; Sivula, K. Evaluating Charge Carrier Transport and Surface States in $CuFeO_2$Photocathodes. *Chem. Mater.* **2017**, *29*, 4952−4962.
(12) Crespo, C. T. Potentiality of $CuFeO_2$-Delafossite as a Solar Energy Converter. *Sol. Energy* **2018**, *163*, 162−166.
(13) Husek, J.; Cirri, A.; Biswas, S.; Asthagiri, A.; Baker, L. R. Hole Thermalization Dynamics Facilitate Ultrafast Spatial Charge Separation in $CuFeO_2$ Solar Photocathodes. *J. Phys. Chem. C* **2018**, *122*, 11300−11304.
(14) Fugate, E. A.; Biswas, S.; Clement, M. C.; Kim, M.; Kim, D.; Asthagiri, A.; Baker, L. R. The Role of Phase Impurities and Lattice Defects on the Electron Dynamics and Photochemistry of $CuFeO_2$ Solar Photocathodes. *Nano Res.* **2019**, *12*, 2390−2399.
(15) Omeiri, S.; Bellal, B.; Bouguelia, A.; Bessekhouad, Y.; Trari, M. Electrochemical and Photoelectrochemical Characterization of $CuFeO_2$ Single Crystal. *J. Solid State Electrochem.* **2008**, *13*, 1395−1401.
(16) Joshi, T.; Senty, T. R.; Trappen, R.; Zhou, J.; Chen, S.; Ferrari, P.; Borisov, P.; Song, X.; Holcomb, M. B.; Bristow, A. D.; Cabrera, A. L.; Lederman, D. Structural and Magnetic Properties of Epitaxial Delafossite $CuFeO_2$ Thin Films Grown by Pulsed Laser Deposition. *J. Appl. Phys.* **2015**, *117*, No. 013908.
(17) Lee, S.; Kang, U.; Piao, G.; Kim, S.; Han, D. S.; Park, H. Homogeneous Photoconversion of Seawater Uranium using Copper and Iron Mixed-Oxide Semiconductor Electrodes. *Appl. Catal. B.* **2017**, *207*, 35−41.
(18) Yoon, S. H.; Han, D. S.; Kang, U.; Choi, S. Y.; Yiming, W.; Abdel-Wahab, A.; Park, H. Effects of Electrochemical Synthetic Conditions on Surface Property and Photocatalytic Performance of Copper and Iron-mixed p-type Oxide Electrodes. *J. Mater. Sci. Technol.* **2018**, *34*, 1503−1510.
(19) Jiang, C.-M.; Reyes-Lillo, S. E.; Liang, Y.; Liu, Y.-S.; Liu, G.; Toma, F. M.; Prendergast, D.; Sharp, I. D.; Cooper, J. K. Electronic Structure and Performance Bottlenecks of $CuFeO_2$ Photocathodes. *Chem. Mater.* **2019**, *31*, 2524−2534.
(20) Hermans, Y.; Klein, A.; Sarker, H. P.; Huda, M. N.; Junge, H.; Toupance, T.; Jaegermann, W. Pinning of the Fermi Level in $CuFeO_2$ by Polaron Formation Limiting the Photovoltage for Photochemical Water Splitting. *Adv. Funct. Mater.* **2020**, *30*, 1910432.
(21) Eyert, V.; Frésard, R.; Maignan, A. Long-Range Magnetic Order and Spin-Lattice Coupling in Delafossite $CuFeO_2$. *Phys. Rev. B* **2008**, *78*, No. 052402.
(22) Zhang, Y.; Kan, E.; Whangbo, M.-H. Density Functional Investigation of the Difference in the Magnetic Structures of the Layered Triangular Antiferromagnets $CuFeO_2$ and $AgCrO_2$. *Chem. Mater.* **2011**, *23*, 4181−4185.
(23) Ferri, M.; Elliott, J.; Farnesi Camellone, M.; Fabris, S.; Piccinin, S. Thermodynamic Stability and Native Point Defects of $CuFeO_2$ Photocathodes in Dry and Electrochemical Environments. *J. Phys. Chem. C* **2019**, *123*, 29589−29598.
(24) Ferri, M.; Elliott, J.; Fabris, S.; Piccinin, S. Establishing Best Practices to Model the Electronic Structure of $CuFeO_2$ from First Principles. *Phys. Rev. B* **2020**, *101*, 155201.
(25) Jiang, T.; Zhao, Y.; Xue, H. Boosting the Performance of Delafossite Photocathode through Constructing a $CuFeO_2$/CuO Heterojunction for Photoelectrochemical Water Reduction. *J. Mater. Sci.* **2019**, *54*, 11951−11958.
(26) Yoon, S. H.; Kang, U.; Park, H.; Abdel-Wahab, A.; Han, D. S. Computational Density Functional Theory Study on the Selective Conversion of CO_2 to Formate on Homogeneously and Heterogeneously Mixed $CuFeO_2$ and CuO Surfaces. *Catal. Today* **2019**, *335*, 345−353.
(27) Baiano, C.; Schiavo, E.; Gerbaldi, C.; Bella, F.; Meligrana, G.; Talarico, G.; Maddalena, P.; Pavone, M.; Muñoz-García, A. B. Role of Surface Defects in CO_2 Adsorption and Activation on $CuFeO_2$ Delafossite Oxide. *Mol. Catal.* **2020**, *496*, 111181.
(28) Giannozzi, P.; Baroni, S.; Bonini, N.; Calandra, M.; Car, R.; Cavazzoni, C.; Ceresoli, D.; Chiarotti, G. L.; Cococcioni, M.; Dabo, I.; Dal Corso, A.; de Gironcoli, S.; Fabris, S.; Fratesi, G.; Gebauer, R.; Gerstmann, U.; Gougoussis, C.; Kokalj, A.; Lazzeri, M.; Martin-Samos, L.; Marzari, N.; Mauri, F.; Mazzarello, R.; Paolini, S.; Pasquarello, A.; Paulatto, L.; Sbraccia, C.; Scandolo, S.; Sclauzero, G.; Seitsonen, A. P.; Smogunov, A.; Umari, P.; Wentzcovitch, R. M. QUANTUM ESPRESSO: a Modular and Open-source Software Project for Quantum Simulations of Materials. *J. Phys. Condens. Matter* **2009**, *21*, 395502.
(29) Giannozzi, P.; Andreussi, O.; Brumme, T.; Bunau, O.; Nardelli, M. B.; Calandra, M.; Car, R.; Cavazzoni, C.; Ceresoli, D.; Cococcioni, M.; Colonna, N.; Carnimeo, I.; Corso, A. D.; de Gironcoli, S.; Delugas, P.; DiStasio, R. A.; Ferretti, A.; Floris, A.; Fratesi, G.; Fugallo, G.; Gebauer, R.; Gerstmann, U.; Giustino, F.; Gorni, T.; Jia, J.; Kawamura, M.; Ko, H.-Y.; Kokalj, A.; Küçükbenli, E.; Lazzeri, M.; Marsili, M.; Marzari, N.; Mauri, F.; Nguyen, N. L.; Nguyen, H.-V.; de-la Roza, A. O.; Paulatto, L.; Poncé, S.; Rocca, D.; Sabatini, R.; Santra, B.; Schlipf, M.; Seitsonen, A. P.; Smogunov, A.; Timrov, I.; Thonhauser, T.; Umari, P.; Vast, N.; Wu, X.; Baroni, S. Advanced

Capabilities for Materials Modelling with Quantum ESPRESSO. *J. Phys. Condens. Matter* **2017**, *29*, 465901.
(30) Hamann, D. R. Optimized Norm-Conserving Vanderbilt Pseudopotentials. *Phys. Rev. B* **2013**, *88*, No. 085117.
(31) Schlipf, M.; Gygi, F. Optimization Algorithm for the Generation of ONCV Pseudopotentials. *Comput. Phys. Commun.* **2015**, *196*, 36−44.
(32) Perdew, J. P.; Burke, K.; Ernzerhof, M. Generalized Gradient Approximation Made Simple. *Phys. Rev. Lett.* **1996**, *77*, 3865−3868.
(33) Anisimov, V. I.; Zaanen, J.; Andersen, O. K. Band theory and Mott insulators: Hubbard U instead of StonerI. *Phys. Rev. B* **1991**, *44*, 943−954.
(34) Anisimov, V. I.; Solovyev, I. V.; Korotin, M. A.; Czyżyk, M. T.; Sawatzky, G. A. Density-Functional Theory and NiO Photoemission Spectra. *Phys. Rev. B* **1993**, *48*, 16929−16934.
(35) Solovyev, I. V.; Dederichs, P. H.; Anisimov, V. I. Corrected Atomic Limit in the Local-Density Approximation and the Electronic Structure of d Impurities in Rb. *Phys. Rev. B* **1994**, *50*, 16861−16871.
(36) Cococcioni, M.; de Gironcoli, S. Linear Response Approach to the Calculation of the Effective Interaction Parameters in the LDA + U Method. *Phys. Rev. B* **2005**, *71*, No. 035105.
(37) Kulik, H. J.; Cococcioni, M.; Scherlis, D. A.; Marzari, N. Density Functional Theory in Transition-Metal Chemistry: A Self-Consistent Hubbard *U* Approach. *Phys. Rev. Lett.* **2006**, *97*, 103001.
(38) Kulik, H. J.; Marzari, N. A Self-Consistent Hubbard U Density-Functional Theory Approach to the Addition-Elimination Reactions of Hydrocarbons on Bare FeO+. *J. Chem. Phys.* **2008**, *129*, 134314.
(39) Guo, Z.; Ambrosio, F.; Chen, W.; Gono, P.; Pasquarello, A. Alignment of Redox Levels at Semiconductor-Water Interfaces. *Chem. Mater.* **2017**, *30*, 94−111.
(40) VandeVondele, J.; Krack, M.; Mohamed, F.; Parrinello, M.; Chassaing, T.; Hutter, J. Quickstep: Fast and Accurate Density Functional Calculations using a Mixed Gaussian and Plane Waves Approach. *Comput. Phys. Commun.* **2005**, *167*, 103−128.
(41) Ambrosio, F.; Miceli, G.; Pasquarello, A. Redox Levels in Aqueous Solution: Effect of van der Waals Interactions and Hybrid Functionals. *J. Chem. Phys.* **2015**, *143*, 244508.
(42) Cheng, J.; Sprik, M. Alignment of Electronic Energy Levels at Electrochemical Interfaces. *Phys. Chem. Chem. Phys.* **2012**, *14*, 11245−11267.
(43) Ambrosio, F.; Guo, Z.; Pasquarello, A. Absolute Energy Levels of Liquid Water. *J. Phys. Chem. Lett.* **2018**, *9*, 3212−3216.
(44) Trasatti, S. The Absolute Electrode Potential: an Explanatory Note (Recommendations 1986). *J. Electroanal. Chem. Interfacial Electrochem.* **1986**, *58*, 955−966.
(45) Goedecker, S.; Teter, M.; Hutter, J. Separable Dual-Space Gaussian Pseudopotentials. *Phys. Rev. B* **1996**, *54*, 1703−1710.
(46) Vydrov, O. A.; Van Voorhis, T. Nonlocal van der Waals Density Functional: The Simpler the Better. *J. Chem. Phys.* **2010**, *133*, 244103.
(47) Sabatini, R.; Gorni, T.; de Gironcoli, S. Nonlocal van der Waals Density Functional Made Simple and Efficient. *Phys. Rev. B* **2013**, *87*, No. 041108.
(48) Miceli, G.; de Gironcoli, S.; Pasquarello, A. Isobaric First-Principles Molecular Dynamics of Liquid Water with Nonlocal van der Waals Interactions. *J. Chem. Phys.* **2015**, *142*, No. 034501.
(49) Ulman, K.; Poli, E.; Seriani, N.; Piccinin, S.; Gebauer, R. Understanding the Electrochemical Double Layer at the Hematite/Water Interface: A First Principles Molecular Dynamics Study. *J. Chem. Phys.* **2019**, *150*, No. 041707.
(50) Bussi, G.; Donadio, D.; Parrinello, M. Canonical Sampling Through Velocity Rescaling. *J. Chem. Phys.* **2007**, *126*, No. 014101.
(51) Choi, D. H.; Moon, S. J.; Hong, J. S.; An, S. Y.; Shim, I.-B.; Kim, C. S. Impurity Dependent Semiconductor Type of Epitaxial $CuFeO_2$ (111) Thin Films Deposited by using a Pulsed Laser Deposition. *Thin Solid Films* **2009**, *517*, 3987−3989 The proceedings of the 1st International Conference on Microelectronics and Plasma Technology (ICMAP 2008)..
(52) Li, S. Z.; Liu, J.; Wang, X. Z.; Yan, B. W.; Li, H.; Liu, J.-M. Epitaxial Growth of Delafossite $CuFeO_2$ Thin Films by Pulse Laser Deposition. *Phys. B* **2012**, *407*, 2412−2415.
(53) Dai, C.; Tian, X.; Nie, Y.; Lin, H.-M.; Yang, C.; Han, B.; Wang, Y. Surface Facet of $CuFeO_2$ Nanocatalyst: A Key Parameter for H_2O_2 Activation in Fenton-Like Reaction and Organic Pollutant Degradation. *Environ. Sci. Technol.* **2018**, *52*, 6518−6525.
(54) Kramer, D.; Ceder, G. Tailoring the Morphology of LiCoO2: A First Principles Study. *Chem. Mater.* **2009**, *21*, 3799−3809.
(55) Humphrey, W.; Dalke, A.; Schulten, K. VMD − Visual Molecular Dynamics. *J. Mol. Graph.* **1996**, *14*, 33−38.
(56) Noguera, C. Polar Oxide Surfaces. *J. Phys. Condens. Matter* **2000**, *12*, R367−R410.
(57) Reuter, K.; Scheffler, M. Composition, Structure, and Stability of RuO_2(110) as a Function of Oxygen pressure. *Phys. Rev. B* **2001**, *65*, No. 035406.
(58) Reuter, K.; Scheffler, M. Composition and Structure of the RuO_2(110) Surface in an O_2 and CO Environment: Implications for the Catalytic Formation of CO_2. *Phys. Rev. B* **2003**, *68*, No. 045407.
(59) Jiang, Y.; Shi, Y.; Xiang, X.; Qi, J.; Han, Y.; Liao, Z.; Lu, T. Thermodynamic Stabilities of Perfect and Vacancy-Defected Li_2TiO_3 (001) Surfaces From First-Principles Analyses. *Phys. Rev. Applied* **2019**, *11*, No. 054088.
(60) Wang, L.; Zhou, F.; Meng, Y. S.; Ceder, G. First-Principles Study of Surface Properties of $LiFePO_4$: Surface Energy, Structure, Wulff Shape, and Surface Redox Potential. *Phys. Rev. B* **2007**, *76*, 165435.
(61) Tsai, C.; Chan, K.; Nørskov, J. K.; Abild-Pedersen, F. Theoretical Insights into the Hydrogen Evolution Activity of Layered Transition Metal Dichalcogenides. *Surf. Sci.* **2015**, *640*, 133−140 Reactivity Concepts at Surfaces: Coupling Theory with Experiment..
(62) Nørskov, J. K.; Rossmeisl, J.; Logadottir, A.; Lindqvist, L.; Kitchin, J. R.; Bligaard, T.; Jónsson, H. Origin of the Overpotential for Oxygen Reduction at a Fuel-Cell Cathode. *J. Phys. Chem. B* **2004**, *108*, 17886−17892.
(63) Hansen, H. A.; Man, I. C.; Studt, F.; Abild-Pedersen, F.; Bligaard, T.; Rossmeisl, J. Electrochemical Chlorine Evolution at Rutile Oxide (110) Surfaces. *Phys. Chem. Chem. Phys.* **2010**, *12*, 283−290.
(64) García-Mota, M.; Bajdich, M.; Viswanathan, V.; Vojvodic, A.; Bell, A. T.; Nørskov, J. K. Importance of Correlation in Determining Electrocatalytic Oxygen Evolution Activity on Cobalt Oxides. *J. Phys. Chem. C* **2012**, *116*, 21077−21082.
(65) Bajdich, M.; García-Mota, M.; Vojvodic, A.; Nørskov, J. K.; Bell, A. T. Theoretical Investigation of the Activity of Cobalt Oxides for the Electrochemical Oxidation of Water. *J. Am. Chem. Soc.* **2013**, *135*, 13521−13530.
(66) Chen, J.; Selloni, A. First Principles Study of Cobalt (Hydr)oxides under Electrochemical Conditions. *J. Phys. Chem. C* **2013**, *117*, 20002−20006.
(67) Nie, X.; Griffin, G. L.; Janik, M. J.; Asthagiri, A. Surface Phases of Cu_2O(111) under CO_2 Electrochemical Reduction Conditions. *Catal. Commun.* **2014**, *52*, 88−91.
(68) Pham, H. H.; Cheng, M.-J.; Frei, H.; Wang, L.-W. Surface Proton Hopping and Fast-Kinetics Pathway of Water Oxidation on Co_3O_4 (001) Surface. *ACS Catal.* **2016**, *6*, 5610−5617.
(69) Cicero, G.; Grossman, J. C.; Catellani, A.; Galli, G. Water at a Hydrophilic Solid Surface Probed by Ab initio Molecular Dynamics: Inhomogeneous Thin Layers of Dense Fluid. *J. Am. Chem. Soc.* **2005**, *127*, 6830−6835.
(70) Kharche, N.; Hybertsen, M. S.; Muckerman, J. T. Computational Investigation of Structural and Electronic Properties of Aqueous Interfaces of GaN, ZnO, and a GaN/ZnO Alloy. *Phys. Chem. Chem. Phys.* **2014**, *16*, 12057−12066.
(71) Van de Walle, C. G.; Martin, R. M. Theoretical Study of Band Offsets at Semiconductor Interfaces. *Phys. Rev. B* **1987**, *35*, 8154−8165.

https://dx.doi.org/10.1021/acscatal.0c05066
ACS Catal. 2021, 11, 1897−1910

(72) Baldereschi, A.; Baroni, S.; Resta, R. Band Offsets in Lattice-Matched Heterojunctions: A Model and First-Principles Calculations for GaAs/AlAs. *Phys. Rev. Lett.* **1988**, *61*, 734−737.
(73) Nozik, A. J. Photoelectrochemistry: Applications to Solar Energy Conversion. *Annu. Rev. Phys. Chem.* **1978**, *29*, 189−222.
(74) Kocha, S. S.; Peterson, M. W.; Arent, D. J.; Redwing, J. M.; Tischler, M. A.; Turner, J. A. Electrochemical Investigation of the Gallium Nitride-Aqueous Electrolyte Interface. *J. Electrochem. Soc.* **1995**, *142*, L238.
(75) Takata, T.; Jiang, J.; Sakata, Y.; Nakabayashi, M.; Shibata, N.; Nandal, V.; Seki, K.; Hisatomi, T.; Domen, K. Photocatalytic Water Splitting with a Quantum Efficiency of Almost Unity. *Nature* **2020**, *581*, 411−414.
(76) van de Krol, R. In *Photoelectrochemical Hydrogen Production*; van de Krol, R., Grätzel, M., Eds.; Springer: Boston, MA, 2012; Chapter 2, pp. 13−65.
(77) Iqbal, A.; Bevan, K. H. Simultaneously Solving the Photovoltage and Photocurrent at Semiconductor-Liquid Interfaces. *J. Phys. Chem. C* **2017**, *122*, 30−43.
(78) Ida, S.; Sato, K.; Nagata, T.; Hagiwara, H.; Watanabe, M.; Kim, N.; Shiota, Y.; Koinuma, M.; Takenaka, S.; Sakai, T.; Ertekin, E.; Ishihara, T. A Cocatalyst that Stabilizes a Hydride Intermediate during Photocatalytic Hydrogen Evolution over a Rhodium-Doped TiO_2 Nanosheet. *Angew. Chem., Int. Ed.* **2018**, *57*, 9073−9077.
(79) Gu, J.; Wuttig, A.; Krizan, J. W.; Hu, Y.; Detweiler, Z. M.; Cava, R. J.; Bocarsly, A. B. Mg-Doped $CuFeO_2$ Photocathodes for Photoelectrochemical Reduction of Carbon Dioxide. *J. Phys. Chem. C* **2013**, *117*, 12415−12422.
(80) Parsons, R. The Rate of Electrolytic Hydrogen Evolution and the Heat of Adsorption of Hydrogen. *Trans. Faraday Soc.* **1958**, *54*, 1053−1063.
(81) Conway, B. E.; Bockris, J. O. Electrolytic Hydrogen Evolution Kinetics and Its Relation to the Electronic and Adsorptive Properties of the Metal. *J. Chem. Phys.* **1957**, *26*, 532−541.
(82) Nørskov, J. K.; Bligaard, T.; Logadottir, A.; Kitchin, J. R.; Chen, J. G.; Pandelov, S.; Stimming, U. Trends in the Exchange Current for Hydrogen Evolution. *J. Electrochem. Soc.* **2005**, *152*, J23.
(83) Greeley, J.; Jaramillo, T. F.; Bonde, J.; Chorkendorff, I.; Nørskov, J. K. Computational High-Throughput Screening of Electrocatalytic Materials for Hydrogen Evolution. *Nat. Mater.* **2006**, *5*, 909−913.
(84) Tang, Q.; Jiang, D.-e. Mechanism of Hydrogen Evolution Reaction on 1T-MoS_2 from First Principles. *ACS Catal.* **2016**, *6*, 4953−4961.
(85) Gauthier, J. A.; Dickens, C. F.; Chen, L. D.; Doyle, A. D.; Nørskov, J. K. Solvation Effects for Oxygen Evolution Reaction Catalysis on IrO_2 (110). *J. Phys. Chem. C* **2017**, *121*, 11455−11463.
(86) Momma, K.; Izumi, F. *VESTA 3*for Three-Dimensional Visualization of Crystal, Volumetric and Morphology Data. *J. Appl. Crystallogr.* **2011**, *44*, 1272−1276.
(87) Amrute, A. P.; LŁodziana, Z.; Mondelli, C.; Krumeich, F.; Pérez-Ramírez, J. Solid-State Chemistry of Cuprous Delafossites: Synthesis and Stability Aspects. *Chem. Mater.* **2013**, *25*, 4423−4435.
(88) Wang, L.; Maxisch, T.; Ceder, G. Oxidation Energies of Transition Metal Oxides within the GGA + U Framework. *Phys. Rev. B* **2006**, *73*, 195107.
(89) Mastrikov, Y. A.; Heifets, E.; Kotomin, E. A.; Maier, J. Atomic, Electronic and Thermodynamic Properties of Cubic and Orthorhombic $LaMnO_3$ Surfaces. *Surf. Sci.* **2009**, *603*, 326−335.
(90) Kim, S.; Aykol, M.; Wolverton, C. Surface Phase Diagram and Stability of (001) and (111) $LiMn_2O_4$ Spinel Oxides. *Phys. Rev. B* **2015**, *92*, 115411.
(91) Li, X.; Hui, Q.; Shao, D.-Y.; Chen, J.-J.; Li, C.-M.; Cheng, N.-P. Stability and Electronic Structure of $MgAl_2O_4$(1 1 1) Surfaces: A First-Principles Study. *Comput. Mater. Sci.* **2016**, *112*, 8−17.
(92) *National Institute of Standard and Technology, U.S. Department of Commerce, NIST-JANAF Thermochemical Tables.* https://janaf.nist.gov/, accessed November 12, 2019.
(93) Nguyen, M.-T.; Seriani, N.; Gebauer, R. Water Adsorption and Dissociation on α-Fe_2O_3 (0001): PBE+U Calculations. *J. Chem. Phys.* **2013**, *138*, 194709.
(94) Mefford, J. T.; Zhao, Z.; Bajdich, M.; Chueh, W. C. Interpreting Tafel Behavior of Consecutive Electrochemical Reactions Through Combined Thermodynamic and Steady State Microkinetic Approaches. *Energy Environ. Sci.* **2020**, *13*, 622−634.

https://dx.doi.org/10.1021/acscatal.0c05066
ACS Catal. 2021, 11, 1897−1910